Wrinkling of Tubes by Axial Cycling

Rong Jiao

Stelios Kyriakides

Research Center for Mechanics of Solids,
Structures and Materials,
WRW 110, C0600,
The University of Texas at Austin,
Austin, TX 78712

Circular tubes compressed into the plastic range first buckle into axisymmetric wrinkling. Initially, the wrinkle amplitude grows with increasing load, but induces a gradual reduction in axial rigidity that eventually leads to a limit load instability and collapse. For lower D/t tubes, the two instabilities can be separated by strain levels of a few percent. Persistent stress-controlled cycling can cause accumulation of deformation by ratcheting. Here, the interaction of ratcheting and wrinkling is investigated. In particular, it is asked if compressive ratcheting can first initiate wrinkling and then grow it to amplitudes associated with collapse. Experiments on SAF2507 super-duplex steel tubes with D/t of 28.5 have shown that a geometrically intact tube cycled under stress control initially deforms uniformly due to material ratcheting. However, in the neighborhood of the critical wrinkling strain under monotonic loading, small amplitude axisymmetric wrinkles develop. This happens despite the fact that the maximum stress of the cycles can be smaller than the critical stress under monotonic loading. In other words, wrinkling appears to be strain rather than stress driven, as is conventionally understood. Once the wrinkles are formed, their amplitude grows with continued cycling, and as a critical value of amplitude is approached, wrinkling localizes, the rate of ratcheting grows exponentially, and the tube collapses. Interestingly, collapse was also found to occur when the accumulated average strain reaches the value at which the tube localizes under monotonic compression. A custom shell model with small initial axisymmetric imperfections, coupled to a cyclic plasticity model, is used to simulate these cyclic phenomena successfully. [DOI: 10.1115/1.4000431]

1 Introduction

Axially loaded circular cylindrical tubes thick enough to enter the plastic range without buckling eventually experience a sequence of instabilities that lead to collapse. The tubes first buckle into an axisymmetric wrinkling mode. With further compression, the wrinkle amplitude steadily grows, while the load increases monotonically. The growth of the wrinkles gradually reduces the axial rigidity of the tube, leading eventually to a limit load instability. Beyond this point, deformation localizes into an axisymmetric lobe. Although in a stiff test fixture the growth of localization can be followed under displacement control loading, the strain at the limit load is the limit state of the structure. For higher diameter-to-thickness (D/t) tubes, the axisymmetric localization can be preceded by a second buckling event where the axisymmetric wrinkling yields to a nonaxisymmetric buckling mode with two, three, or more circumferential waves. This also leads to a limit load instability and localization and consequently becomes the limit state (see Lee [1], Batterman [2], Gellin [3], Bushnell [4], Tvergaard [5,6], Yun and Kyriakides [7], Bardi and Kyriakides [8], Bardi et al. [9], and Kyriakides and Corona [10]).

This study is concerned with a related problem where the tube is loaded cyclically. It is well known that metals cycled under stress control about a mean stress into the plastic range accumulate deformation with every cycle, or *ratchet* (see Hassan and Kyriakides [11], Hassan et al. [12] and their references). Thus, if the mean stress is compressive, ratcheting causes progressive compression to the tube. In a previous investigation, we showed that ratcheting can cause the amplitude of pre-existing wrinkles to grow and that persistent cycling can lead to localization of wrinkling and collapse (Jiao and Kyriakides [13]). Here, we investigate whether wrinkling can be initiated by compressive strain accumulated by ratcheting, even though the maximum compressive stress seen during the cycling is significantly lower than the critical stress required to wrinkle the tube under monotonic compression.

The investigation, although of broader and fundamental interest, is motivated by the following practical problem that can affect offshore pipelines used to transport hydrocarbons. In many places, pipelines installed on the sea floor must be buried in trenches. In such situations, the lines are axially restrained, and the passage of hot hydrocarbons at a relatively high pressure can plastically deform the pipe (Klever et al. [14]). During a lifetime of 20–30 years, pipelines are shut down for maintenance and other reasons and are restarted several times (a few hundred cycles). Thus, the question arises as to whether ratcheting that results from this cycling can wrinkle the pipe or, even worse, if it can eventually cause failure.

Despite their importance in applications such as earthquake resistant structures, nuclear reactor components, offshore structures under extreme weather conditions, etc., fundamental studies on the degradation of structures under cyclic loadings are surprisingly scarce. Kyriakides and Shaw [15], Corona and Kyriakides [16], and Chang and Pan [17] reported degradation of tubes under cyclic bending in the form of accumulated ovalization that eventually causes collapse. Ellison and Corona [18], Vaze and Corona [19], and Yin et al. [20] reported gradual degradation and localized collapse of beams of various cross sections under cyclic bending. Goto et al. [21] and Corona [22] reported numerical results on localization of transverse deflection in a periodically supported column undergoing cycling. In the majority of these studies, the structures were cycled under "displacement" control. By contrast, the present body of work investigates axial cycling under load control where ratcheting can enhance the induced degradation. The buried pipeline problem mentioned above has its own rather complex biaxial cyclic loading history. Thus, the axial cycling examined here and in the preceding paper [13] contributes to only part of the solution to this practical problem.

The problem will be first investigated experimentally following the methodology established in Ref. [13]. Tubes will be first com-

---

Contributed by the Applied Mechanics Division of ASME for publication in the JOURNAL OF APPLIED MECHANICS. Manuscript received April 28, 2009; final manuscript received August 5, 2009; published online February 23, 2010. Review conducted by Robert M. McMeeking.

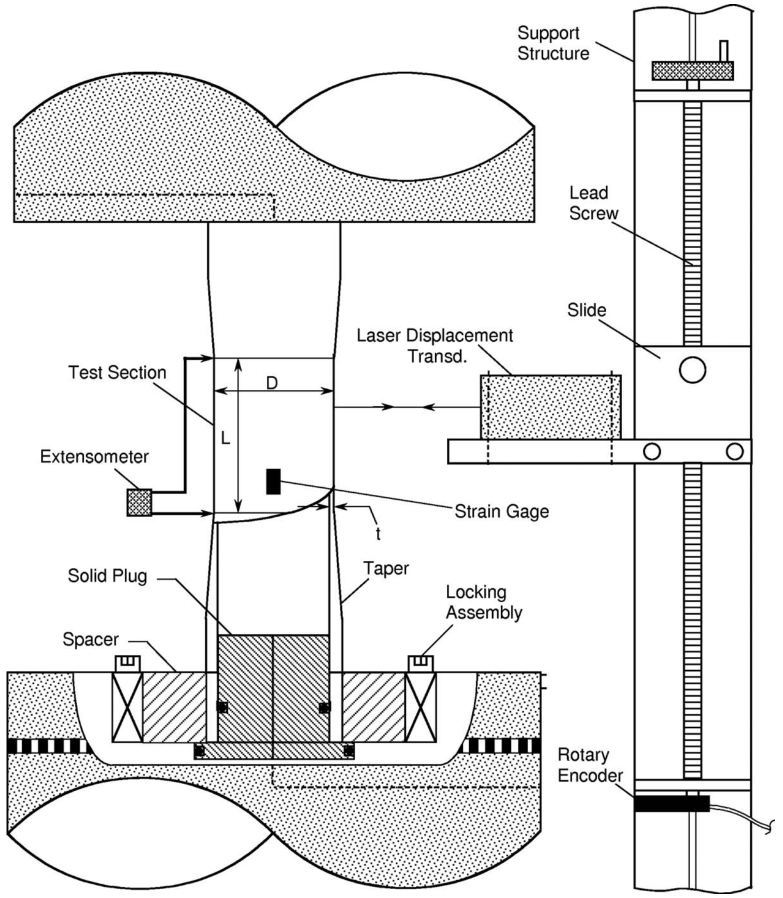

Fig. 1 Scaled schematic of the experimental setup used

pressed monotonically into the plastic range stopping well before the critical wrinkling strain. The tubes will then be cycled under load control about a compressive mean stress, as a consequence causing material ratcheting. The ratcheting will be followed well past the strain levels at which the tube wrinkles under monotonic loading in order to establish if the accumulated strain wrinkles the tube. The experiments will also be simulated numerically using the formulation and nonlinear kinematic hardening constitutive model framework developed in Ref. [13].

2 Experimental

2.1 Experimental Setup and Procedures. The circular tubes tested are similar to those used in the monotonic buckling experiments of Bardi and Kyriakides [8] and in the recent cyclic experiments of Ref. [13]. They were machined out of an SAF 2507 super-duplex seamless tube stock (60.3 mm (2.375 in.) outside diameter and 3.91 mm (0.154 in.) wall). In order to reduce geometric imperfections, both the internal and external surfaces of the tubes were machined, trying to keep the finished surfaces parallel with minimum wall eccentricity (typical tolerance of 0.025 mm ($\sim$0.001 in.)). The test section has an outside diameter of approximately 57.2 mm (2.25 in.), a length of 76 mm (3.0 in.), and a wall thickness of about 1.98 mm (0.078 in.). Linear tapers connect the test section to thicker end segments that are left at the as-received diameter (see Fig. 5 in Ref. [13]). The length of the tapers was selected through finite element (FE) simulations of the test setup so as to minimize the effect of the thickness discontinuities on the axial stress. The taper geometry chosen resulted in an overall specimen length of 298 mm (11.75 in.). This choice of specimen geometry implies that the onset and growth of wrinkling would be approaching that expected of a long uniform tube.

The specimens were preloaded and cycled in a 1 MN (225 kip) servohydraulic testing machine that can be operated in displacement or load control. The test setup is shown in a scaled schematic in Fig. 1. The thicker parts of the specimen engage custom axisymmetric grips that include Ringfeder locking assemblies and solid brass end plugs. A custom extensometer that spans the test section is used to measure its change in length. In monotonic compression tests, the axial strain in the test section was also monitored by strain gauges.

A scanning device is used to periodically scan the surface of the test section during the test. The device consists of a noncontact laser displacement transducer mounted on a lead screw-driven slide. The slide is equipped with a rotary encoder that allows monitoring of the axial position of the transducer (see Fig. 1). The transducer (Keyance LK-G82) sends a beam to the surface of the specimen; the reflection passes through a lens system and is received by a Li charge coupled device (CCD) that is at some distance from the source of the emitted beam. The displacement of the reflecting surface is then evaluated by triangulation. The specific transducer used has a range of 80 ± 15 mm (3.15 ± 0.59 in.) and was operated at a resolution of 1 μm with a spot size of about 70 μm. The transducer is operated by a LK-G controller, and the resultant DC output is received in a LabVIEW based data acquisition system. The instrument operates at 50 kHz.

The surface is scanned axially along a generator by manually rotating the slide lead screw in the process traversing the transducer. The lead screw thread (20 threads per inch) combined with the encoder (HEDS5500-A06 with 500 CPR-counts per revolution) provides an axial resolution of 10^{-4} in. (10,000 counts/in.).

Table 1 Specimen parameters and critical variables measured in monotonic axial buckling experiments

Expt. no.	D mm (in.)	t mm (in.)	$\frac{D}{t}$	$t_{\min}-t_{\max}$ mm (in.)	σ_C MPa (ksi)	ε_C (%)	$\frac{\lambda_C}{R}$	σ_L MPa (ksi)	$\bar{\varepsilon}_L$ (%)
CWR20	57.24 (2.2536)	1.99 (0.0785)	28.71	1.98–2.02 (0.0778–0.0794)	700–715.9 (101.5–103.8)	1.15–1.45	0.224–0.300	805.5 (116.8)	4.50
CWR21	57.23 (2.2531)	1.99 (0.0785)	28.70	1.98–2.00 (0.0778–0.0788)	607.2–720.7 (101.1–104.5)	1.15–1.60	0.264–0.326	794.5 (115.2)	4.42

The count is performed using a PCI-QUAD04 PC card that operates in conjunction with a LabVIEW subroutine. The resultant displacement is recorded in the data acquisition system on a common time base with the laser transducer output.

In monotonic compression tests, the specimen was first scanned at zero load and at regular intervals during the loading. In the cyclic experiments, the specimen was scanned several times during the monotonic part of the loading and every 10–15 cycles during cycling. The high resolution of the transducer makes it sensitive to surface roughness and vibrations. The noise was reduced by mounting the instrument and the slide on a stiff support structure (only shown partially in Fig. 1). Despite this improvement, the signals still exhibited some high frequency noise that had to be filtered out.

2.2 Monotonic Compression Tests. Two tubes were compressed monotonically to collapse at a constant displacement rate that resulted in a strain rate of approximately 3×10^{-5} s^{-1}. The geometric parameters of the tubes are listed in Table 1. Figure 2 shows one of the recorded nominal stress (σ_x)-shortening (δ_x/L, $L\equiv$gauge length) responses for a tube with $D/t=28.71$. Figure 3(*a*) shows a 3D rendering of a set of axial scans of the radial displacement along a generator (w/R) of the surface of the test section at different average strains ($\bar{\varepsilon}_x\equiv\delta_x/L$; note that here we are interested in the evolution of the wrinkles, and consequently the mean value of w was reduced for a clearer presentation). The scans correspond to the locations marked with solid bullets on the response in Fig. 2. The results are similar to those reported in Ref. [8]. Initially, the test section deforms uniformly, and the axial displacement scans change very little. Signs of the gradual growth of small initial imperfections can be seen in the scan at $\bar{\varepsilon}_x=1.0\%$. By an average strain of 1.15%, the scan starts to show a wavy pattern that becomes even clearer at $\bar{\varepsilon}_x=1.45\%$. At even higher average strains, the wavy patterns become fully developed with clear peaks and valleys as the tube is wrinkled in a nearly axisymmetric manner. The amplitude of the wrinkles grows with compression, and in the process the axial stiffness of the tube gradually reduces. At the same time, the amplitudes of the wrinkles at the ends of the test section start to grow faster (see selected scans in Fig. 3(*b*)). At an average strain of 4.5%, a load maximum develops, causing deformation to localize further this time on the left hand side of the specimen. The experiment was interrupted at $\bar{\varepsilon}_x=5.2\%$ and unloaded. The last scan included in Fig. 3(*b*) was recorded just prior to unloading.

As in Bardi and Kyriakides [8], we will associate the first signs of wrinkling with the value yielded by a plastic bifurcation analysis associated with an axisymmetric buckling mode (i.e., the mathematical idealization of buckling; see Ref. [23]). In this case, our best estimate of the onset of wrinkling is that it is bounded between strains of 1.15% and 1.45%, marked with arrows (↓) on the response in Fig. 2. The corresponding stresses are included in Table 1 under σ_C. The bounds for ε_C are included in Fig. 4 (using ◆ ◇), where similar experimental results from Bardi and Kyriak-

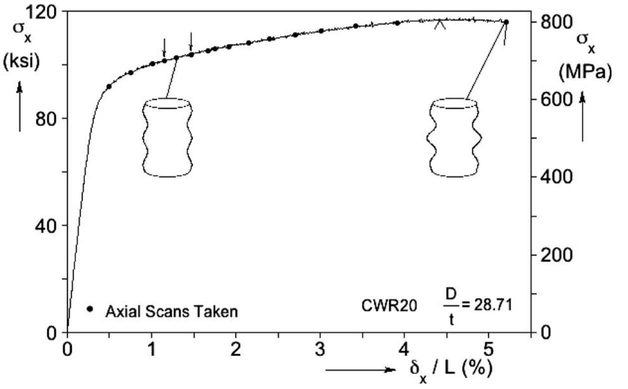

Fig. 2 Typical stress-shortening response from a monotonic compression test of an inelastic circular cylindrical shell. Marked are the onset of wrinkling (↓) and the limit load (ˆ), followed by localization and collapse.

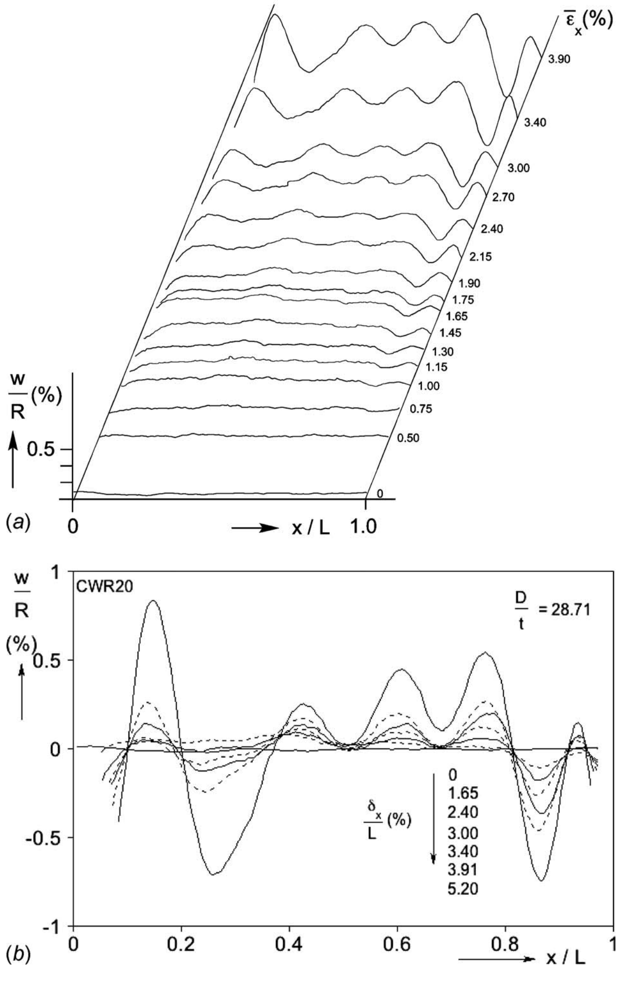

Fig. 3 (*a*) Radial displacement axial profiles recorded at different average strain levels during the monotonic compression test in Fig. 2 that show the evolution of the wrinkles. (*b*) Axial scans showing the evolution of wrinkles and their localization at higher strain levels.

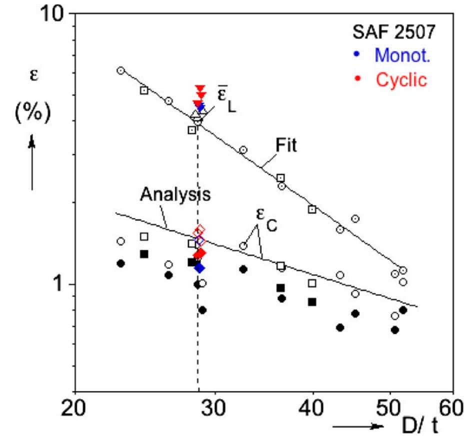

Fig. 4 Critical wrinkling strains (ε_C) and average limit strains ($\bar{\varepsilon}_L$) versus *D/t* from 15 experiments of Bardi and Kyriakides [8] and several new experiments with *D/t*≅28.5

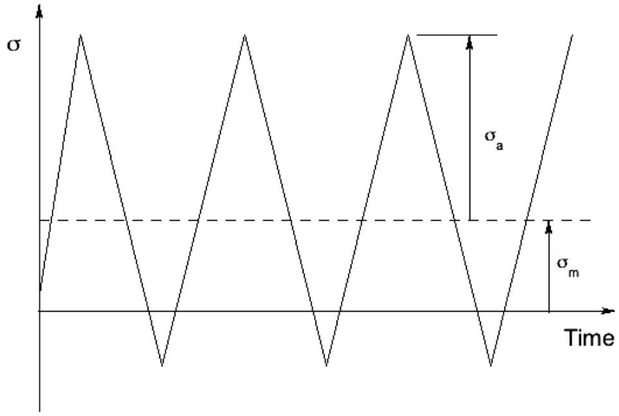

Fig. 5 Cyclic stress history applied in the experiments

ides [8] are plotted versus D/t on log-log scales. The corresponding calculated critical strain is drawn with a solid line. The two sets of new results are seen to follow the trend of the previous results.

The recorded stress maximum and the corresponding strain ($\bar{\varepsilon}_L$) are associated with the onset of collapse. The data from the two new experiments are also included in Fig. 4 (using ▼), where again they are seen to be in reasonable agreement with the results of Ref. [8] as well as the recent ones of Ref. [13]. Thus, the onset of wrinkling is separated from collapse by an average strain of about 3%. The wavelengths of the wrinkles (2λ) were measured and found to also vary within a range partly influenced by the finiteness of the test section (see Table 1). The wavelengths are again in line with those reported in Ref. [8].

2.3 Cyclic Experiments. Three cyclic experiments with the major problem parameters listed in Table 2 were performed as follows: each tube was first compressed monotonically into the plastic range under displacement control to a strain ($\varepsilon_{\text{xmon}}$) that was significantly smaller than the strain level at which the tube showed the first signs of wrinkling under monotonic loading (ε_C in Table 1); in other words, ensuring that the tube was free of wrinkles. The machine was then switched to load control, and the tube was cycled axially with an amplitude of σ_a about a compressive mean stress σ_m, following the triangular history shown in Fig. 5 (cycle period=120 s). The two stress levels were chosen such that the maximum compressive stress in the cycle corresponded to the value at which the specimen was unloaded from during the initial monotonic phase of the loading history (σ_{xmon} in Table 2). The minimum was set at a level that the cycle would induce material ratcheting. We note that these cycle variables determine the rate of material ratcheting.

A representative stress-displacement response recorded in experiment CWR19 is shown in Fig. 6. In this case, $(\varepsilon_{\text{xmon}}, \sigma_{\text{xmon}})=(0.99\%, 691\ \text{MPa}—100.2\ \text{ksi})$, and the loading parameters of the first 410 cycles were $(\sigma_a, \sigma_m)=(510, 180.6)$ MPa, $(74.0, 26.2)$ ksi. The ratcheting induced by cycling is clearly visible in the figure, where the (average) strain ($\delta_x/L \equiv \bar{\varepsilon}_x$) at the end of 410 cycles is seen to reach a value of 2.29%. The cycling was interrupted every 10 cycles or 15 cycles in order to perform an axial scan of the test section, as described earlier (scans taken at the mean stress of the cycle). Figure 7 shows a select number of the axial scans plotted in the same manner as in the monotonic experiment shown in Fig. 3(*a*). Here, the scans are identified by the average strain of the cycle ($\bar{\varepsilon}_x$) and the number of the cycle (N). Included are scans taken before the test at zero load (0:0) and ones at strains of 0.7% and 0.99% before the cycling commenced, identified by (0.7:0) and (0.99:0), respectively. These scans show the presence of very small initial imperfections that get slightly, if at all, amplified by the compressive stress. In the first scan during the cycling, taken after 10 cycles (1.08:10), the surface profile has changed little. In the next scan shown (1.30:40), the first signs of a wavy pattern start to emerge, and the wrinkles become fully developed by cycle 110 when $\bar{\varepsilon}_x$ reached a value of 1.60%. Thus, the onset of wrinkling is bounded by strain levels of 1.30% and 1.60%. Subsequently, as the tube is further compressed by the ratcheting, the wrinkle amplitude is seen to grow. This phase of the test was terminated at (2.29:410).

It is useful to compare the strain at the onset of wrinkling with the corresponding critical strains measured under monotonic loading. The two bounds of (1.30% and 1.60%) are included in Table 2, where they are seen to be in good agreement with the corresponding bounds for the two monotonic tests in Table 1. The two bounding strains are also included in Fig. 4, where they are seen to fall in line with other data for this tube D/t. The wrinkle wavelengths of CWR19 were found to be in the range of $\lambda/R \in (0.262, 0.368)$ (see Table 2). Once more, these values are in reasonable agreement with the corresponding values from the monotonic tests in Table 1. In other words, *the tube buckles into an axisymmetric mode at about the same strain and with about the*

Table 2 Geometric and material parameters of wrinkling under cyclic loading experiments

Expt. no.	D mm (in.)	t mm (in.)	$\frac{D}{t}$	σ_{xmon} MPa (ksi)	$\varepsilon_{\text{xmon}}$ (%)	σ_{m1} MPa (ksi)	σ_{a1} MPa (ksi)	N_1	$\bar{\varepsilon}_1$ (%)	ε_C (%)	σ_{m2} MPa (ksi)	σ_{a2} MPa (ksi)	N_C	$\bar{\varepsilon}_f$ (%)	$\frac{\lambda}{R}$
CWR15	57.20 (2.2520)	1.98 (0.0781)	28.83	678.0 (98.31)	0.80	167.6 (24.31)	510.0 (74.00)	410	1.90	1.30–1.45	219.9 (31.89)	510.0 (74.00)	609	4.93	0.255–0.372
CWR18	57.23 (2.2532)	2.00 (0.0788)	28.60	677.2 (98.19)	0.92	166.8 (24.19)	510 (74.00)	490	2.14	1.28–1.55	220.0 (31.90)	510.0 (74.00)	632	4.62	0.325–0.373
CWR19	57.21 (2.2524)	1.99 (0.0782)	28.80	691.1 (100.2)	0.99	180.6 (26.21)	510 (74.00)	410	2.29	1.30–1.60	234.1 (33.94)	510.0 (74.00)	607	5.23	0.262–0.368

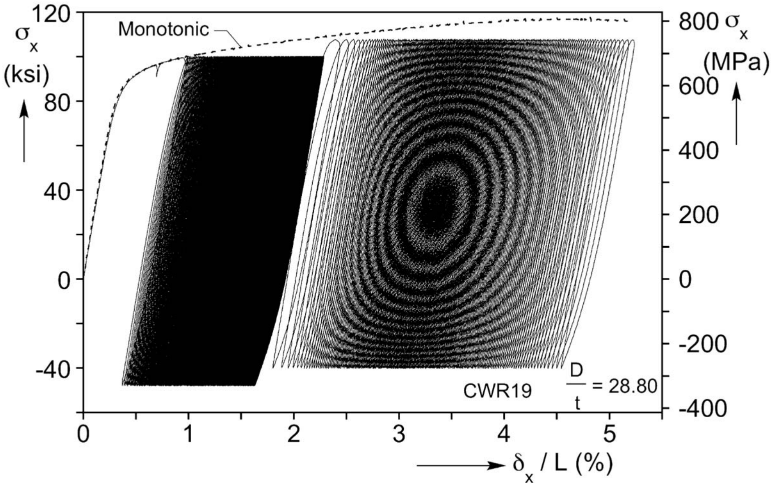

Fig. 6 Axial stress-shortening response from cyclic loading experiment CWR19

same wavelength as it does under monotonic loading. This happens despite the fact that the stress level at the onset of wrinkling is 691 MPa (100.2 ksi), whereas under monotonic loading it was about 707–717 MPa (102–104 ksi). It would thus seem that this type of plastic buckling is strain driven, which goes against the conventional understanding that it is stress driven.

Once the wrinkles are fully developed, the test becomes similar to the ones in Ref. [13] where the effect of ratcheting on prewrinkled tubes was examined. Jiao and Kyriakides [13] reported that stress-controlled cycling of prewrinkled tubes causes the amplitude of the wrinkles to grow and eventually leads to localization of wrinkling and collapse. In the present test, the initial rate of ratcheting is relatively slow, and in view of this background, the cycle parameters were altered in order to increase it so as to reach collapse in a more reasonable number of cycles. Hence, the cycle mean stress was increased to 234 MPa (33.94 ksi). This choice resulted in a maximum cycle stress of 744 MPa (107.9 ksi), a value that corresponds to the monotonic loading stress at the current strain of 2.29% (see Fig. 6). 197 additional cycles were performed with the new cycle parameters. The higher mean stress increased the rate of ratcheting considerably, reflected by the wider stress-"strain" loops traced. When the average strain reached approximately 4%, wrinkling localized initially at the two ends and subsequently at the end on the left hand side of the specimen (Fig. 7). The test was terminated on cycle 607 when the localized wrinkle was deemed to be close to collapsing.

The rate of axial ratcheting is also depicted in Fig. 8, where the peak displacement (δ_x^p/L) in each cycle is plotted against the number of the cycle N. Following an initial transient that lasts about

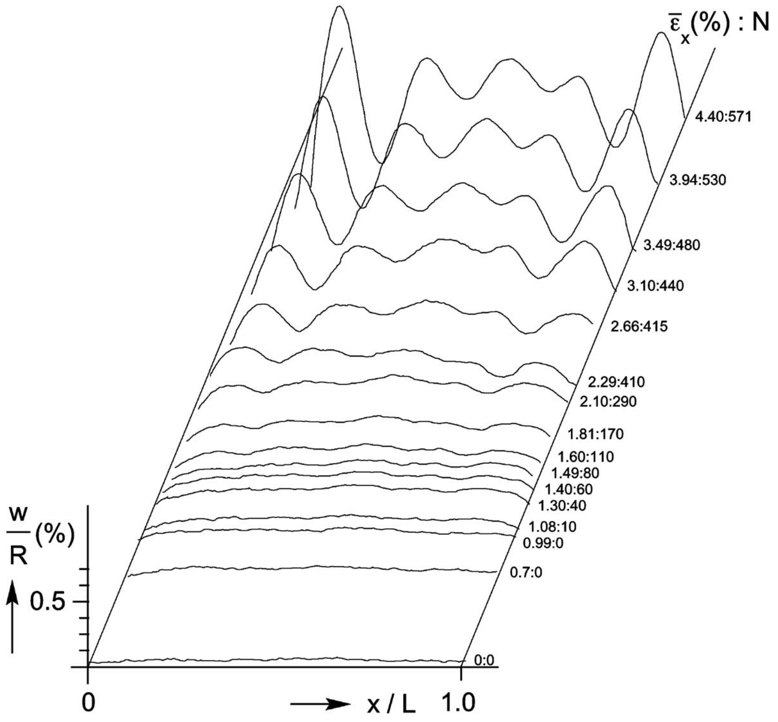

Fig. 7 Radial displacement axial profiles after different numbers of cycles showing the growth and localization of wrinkles for CWR19

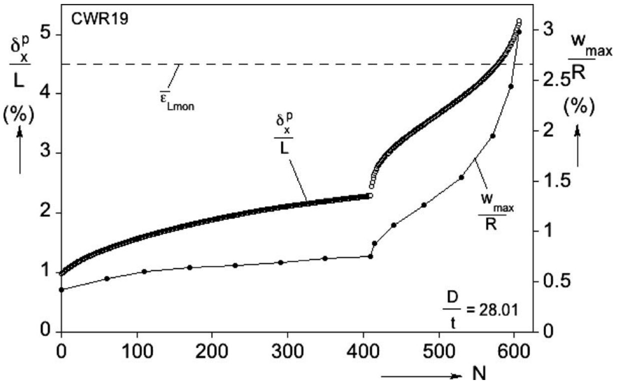

Fig. 8 Peak axial displacement per cycle versus *N* and corresponding maximum radial displacement in wrinkles for CWR19

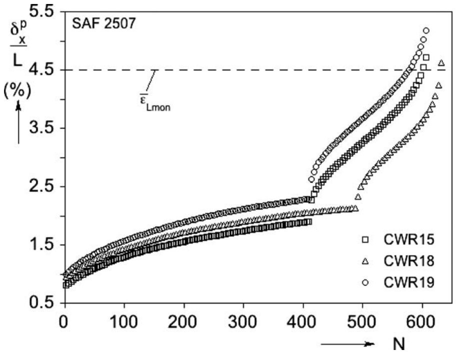

Fig. 9 Peak displacement per cycle versus *N* from three experiments with slightly different initial prestraining

75 cycles, the rate of ratcheting settles to a nearly constant rate (it actually gradually slows down slightly). During the first 100 or so cycles when the test section is essentially free of wrinkles, δ_x^p/L corresponds to the ratcheting strain. Subsequently, δ_x^p is partly due to material strain and partly due to shortening caused by the growth of the amplitude of the wrinkles.

Included in Fig. 8 is the radial displacement ($w_{\max}$) versus N measured at the location of the dominant wrinkle (i.e., on the left hand end in Fig. 7). The trend of the growth of this variable is similar to that of δ_x^p. Once more, before the initiation of wrinkles, $w_{\max}/R$ corresponds to the hoop strain, which is approximately $0.5\varepsilon_x$. When the wrinkles develop, the radial displacement is partly due to the material ratcheting and partly due to the wrinkle amplitude. The higher mean stress of the second part of the test is seen to increase both the rate of growth of δ_x^p and $w_{\max}$ considerably. Both variables exhibit an initial transient, then settle to a constant rate of growth, and around cycle 530 start to grow at a faster rate that becomes exponential during the last 50 or so cycles. The test was terminated when the average strain reached a value of 5.23% (depicted as $\bar{\varepsilon}_f$ in Table 2).

Included in Fig. 8 with a horizontal dashed line is the average strain at which the tubes collapsed under monotonic loading ($\bar{\varepsilon}_{\text{Lmon}}$). We can see that this strain level corresponds to the strain at which the cycled tube experiences exponential growth in both δ_x^p and $w_{\max}$. In other words, under this type of cyclic loading, the tube tends to collapse at approximately the same average strain as it does under monotonic loading. This occurs despite the stress level in the cyclic test being 744 MPa (107.9 ksi) versus about 800 MPa (116 ksi) for monotonic tests. This conclusion is in concert with a similar one in Ref. [13] and once more points to the onset of localization being a strain-driven instability. It is also reminiscent of experimental results in Corona and Kyriakides [16] involving moment-controlled cyclic bending of Al-alloy tubes that induces a ratcheting of curvature and a simultaneous accumulation of ovalization. It was found that the cycled tubes collapsed when the curvature at which they collapsed under monotonic bending was reached.

Two additional cyclic experiments were conducted (CWR15 and CWR18) with approximately the same geometric and loading parameters (see Table 2). CWR15 was compressed monotonically to a strain of 0.80%. It was then cycled with an amplitude and mean stress of 510 MPa and 168 MPa (74.0 ksi and 24.31 ksi), respectively, for 410 cycles. The behavior was very similar to the one reported above, and thus detailed results will not be shown. The recorded maximum displacement in each cycle is plotted against N in Fig. 9 along with the results for the other two experiments. The somewhat smaller $\varepsilon_{\text{xmon}}$ and σ_a result in a slightly lower rate of ratcheting. Wrinkles became discernible between strain levels of 1.30% and 1.45%, in other words, in the same neighborhood as they did for CWR19 and for the monotonic loading experiments. After cycle 410, at $\delta_x^p/L=1.90\%$, the mean stress was increased to 220 MPa (31.89 ksi), and 199 additional cycles were applied. The results in Fig. 9 show that after about cycle 550, the rate of ratcheting accelerated and showed clear signs of approaching collapse when δ_x^p/L reached a value of 4.5%, which again corresponds to the onset of collapse under monotonic loading. The third experiment (CWR18) had slightly different values of $\varepsilon_{\text{xmon}}$ and σ_m (Table 2), and consequently the rate of ratcheting is somewhat higher than that of CWR15. The first phase of the test involved 490 cycles, reaching an average strain of 2.14%. The specimen showed signs of wrinkling between strains of 1.28% and 1.55%. The second phase of the test had $\sigma_m=220$ MPa (31.90 ksi) and lasted for 142 cycles. Once more, at around an average strain of 4.5%, the specimen showed signs of approaching collapse. The test was terminated at an average strain of 4.62%.

Thus, in summary, all three cyclic experiments show similar trends. Strain induced by ratcheting induces axisymmetric wrinkling at approximately the same strain that wrinkles tend to appear under monotonic compression. Furthermore, the wrinkle wavelengths under cyclic loading are of the same order of magnitude as those measured in monotonic loading tests. These events take place despite the fact that the stress in the cyclic experiments was consistently lower than the critical stress under monotonic loading. This indicates that the onset of plastic wrinkling is deformation rather than stress driven. Shells always have small initial imperfections, which in the present case can be considered to have a somewhat random distribution. These imperfections get accentuated by compression. It appears that as the critical strain is approached, the minimum energy wavelengths get excited and grow faster than other wavelengths. The dominant wrinkles tend to grow with further straining by ratcheting. At an average strain that is again similar to the value at which the shell tends to localize and collapse under monotonic loading, wrinkling localizes and the shell collapses very much as if it was loaded monotonically.

3 Analysis

3.1 Formulation. The problem of plastic buckling of long circular cylinders under axial compression was fully addressed by Bardi et al. [9] (see also Ref. [7]). Jiao and Kyriakides [13] adopted the axisymmetric version of this formulation, coupled it to a cyclic plasticity constitutive model, and used them to simulate the evolution of wrinkling in the prewrinkled tubes tested. Here, we will adopt the same formulation and constitutive model and attempt to simulate the ratcheting and subsequent wrinkling observed in the present experiments. To avoid repetition, only an outline of this formulation will be presented. In the same spirit, only elements of the constitutive model essential in its calibration will appear in Appendix. For more details on the modeling, the reader is referred to Ref. [13].

Table 3 Constitutive model parameters

Loading	E GPa (Msi)	E_o^p GPa (ksi)	σ_o MPa (ksi)	σ_b MPa (ksi)	a GPa (Msi)	b	γ	k	C_r
Monot.	195 (28.2)	4.14 (600)	428 (62.0)	675 (97.9)	86.2 (12.5)	0	0	0.1	40
Cyclic	195 (28.2)	4.14 (600)	328 (47.5)	745 (108.1)	2069 (300)	36	3	0.1	40

$S_\theta=1.15$; $S_r=0.85$. See Ref. [13].

We again consider a thin-walled circular cylindrical shell with midsurface radius R, wall thickness t, and length $2L$, which is compressed and cycled in the same manner as in the experiments. As in the experiments, the shell will be initially compressed sufficiently to enter the plastic range and then cycled under load control with a mean compressive stress, inducing cyclic plastic deformation by ratcheting. Rather than seeking the onset of wrinkling through a bifurcation analysis, as is customary for monotonic loading, we introduce a very small initial axisymmetric imperfection of the form,

$$\bar{w}=t\left[\omega_o+\omega_1\cos\left(\frac{\pi x}{N\lambda}\right)\right]\cos\left(\frac{\pi x}{\lambda}\right) \tag{1}$$

where 2λ is the wavelength of the wrinkling buckling mode under monotonic loading (see Ref. [23]), and the shell domain is $2L=2N\lambda$. ω_o is the amplitude of this imperfection, and ω_1 is the amplitude of a bias toward $x=0$. The strains at any point on the shell are given by

$$\varepsilon_{\alpha\beta}=(\varepsilon^o_{\alpha\beta}+z\kappa_{\alpha\beta})/(A_\alpha A_\beta)^{1/2}, \quad \text{where } A_1\cong 1, \quad A_2\cong 1+\frac{z}{R} \tag{2a}$$

and the appropriate strain-displacement equations are

$$\varepsilon^o_{xx}=u,_x+\frac{1}{2}w,_x^2, \quad \varepsilon^o_{\theta\theta}=\frac{w}{R}, \quad \kappa_{xx}=-w,_{xx} \tag{2b}$$

Equilibrium will be satisfied through the principle of virtual work (PVW), which by assuming symmetry about the midspan can be written as

$$2\pi R\int_0^L\{N_{xx}\delta\varepsilon^o_{xx}+N_{\theta\theta}\delta\varepsilon^o_{\theta\theta}+M_{xx}\delta\kappa_{xx}\}dx=\delta W \tag{3}$$

where $N_{\alpha\beta}$ and $M_{\alpha\beta}$ are the membrane and bending moment intensities. The problem domain is discretized by adopting the following admissible expansions for the displacements:

$$w=a_0+\sum_{n=1}^{N_w}a_n\cos\left(\frac{n\pi x}{N\lambda}\right) \quad \text{and} \quad u=b_0x+\sum_{n=1}^{N_u}b_n\sin\left(\frac{n\pi x}{N\lambda}\right) \tag{4}$$

Thus, $b_0=\delta_x/N\lambda$ is the average axial strain, and in Eq. (3) $\delta W=PN\lambda\delta b_0$ for load-controlled loading and $\delta W=0$ for displacement-controlled loading. The resultant nonlinear equations are solved using the Newton–Raphson method.

The elastoplastic cyclic behavior of SAF2507 super-duplex steel is modeled using the two-surface nonlinear kinematic hardening model of Dafalias and Popov [24,25] with the modifications introduced for ratcheting in Hassan et al. [12], Hassan and Kyriakides [11,26,27] (this material is essentially cyclically stable and is modeled as such). An outline of this model is presented in the Appendix. The calibration of the model is described in Sec. 3.3 of Ref. [13].

3.2 Simulation of Cyclic Experiments. The model outlined is now used to simulate the cyclic experiments presented. We start with a simulation of CWR19 using the geometric parameters listed in Table 2. The tubes are plastically anisotropic with $\{S_r,S_\theta\}$ values given below Table 3 (see Ref. [13] for definitions). Using these anisotropies, the critical wrinkle half wavelength was evaluated to be $\lambda=0.300R$ using the procedure in Ref. [23]. The imperfection amplitudes $\{\omega_o,\omega_1\}$ were chosen for optimal performance of the model, which in this case were found to be {0.02%, 0.02%}. A shell length $2L=14\lambda$ will be adopted in all calculations.

This tube was precompressed to $\bar{\varepsilon}_{\text{xmon}}=0.99\%$. The constitutive model parameters used for this part of the loading history come from the initial monotonic stress-strain response of the material and are listed under Monot. in Table 3. The parameters used for the stress-controlled cycling come from the stable hysteresis and appear in the same table under Cyclic. The parameters are the same as those used in Ref. [13] except for a smaller value of σ_b due to the cycling starting at a smaller prestrain and a smaller value of C_r chosen for better performance of the model (see the parameter sensitivity study in Sec. 3.3 and the definition of optimal performance).

The calculated stress-shortening response is shown in Fig. 10. Following the initial preloading, the model was cycled axially using the cycle variables $\{\sigma_{a1},\sigma_{m1}\}$ of the experiments (Table 2). A total of 410 cycles were applied during which the tube ratcheted to $\delta_x^p=0.0235L$. The characteristics of the calculated response are very similar to those of the corresponding experimental one in Fig. 6. Figure 11 shows plots of the calculated peak axial displacement (δ_x^p/L) and the maximum radial displacement in each cycle $(w_{\max}(0)/R)$ versus N along with the corresponding experimental results (note that the plane of symmetry is at $x=0$). Both sets of predictions are seen to be in very good agreement with the measurements. Both replicate the initial transient that lasts about 100 cycles and then settle into a nearly constant rate of growth maintaining approximately a ratio of 0.5 expected from incompressibility. Clearly, the main contributor here is material ratcheting; however, simultaneously, the wrinkle amplitude grows gradually. Figure 12 shows a set of deformed generators at different average strains and N during the loading history. After 10 cycles, when the average strain is 1.02%, the wrinkles are barely discernible. By cycle 67 and an average strain of about 1.5%, they have grown slightly and become more pronounced by cycle 170 when $\bar{\varepsilon}_x=1.89\%$. Thus, by the end of this phase of loading history at $N=410$ and $\bar{\varepsilon}_x=2.35\%$, the wrinkles are fully developed very much as was the case in the experiment.

As in the experiment, the $w_{\max}-N$ plot in Fig. 11 does not show any sudden change in its rate of growth, making it difficult to pinpoint any strong tendency of the wrinkled solution becoming dominant (remember that for monotonic loading the bifurcation is tangential to the trivial solution). Included in the figure with a dashed line is the critical bifurcation strain calculated for this tube, assuming that the loading was monotonic (this is also marked with an arrow (←) in Fig. 12(*a*)). Clearly, this strain level is in reasonable agreement with the neighborhood in which the wrinkles start to become discernible in Fig. 12(*a*).

The same constitutive model parameters were used to simulate the second phase of the experiment with the higher mean stress ($\sigma_{m2}=234$ MPa—33.94 ksi). A total of 200 additional cycles were applied, and the results are included in Figs. 10–12. The structure ratchets at a higher rate, and this is reflected in the stress-displacement response in Fig. 10 and in the $\delta_x^p/L-N$ and $w_{\max}$

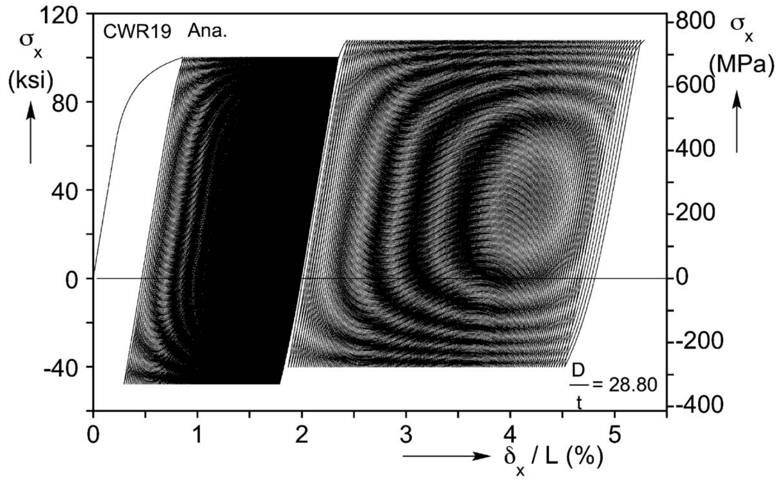

Fig. 10 Calculated axial stress-shortening response for CWR19

$-N$ plots in Fig. 11. All sets of predictions are seen to follow the experimental results quite closely. At the same time, the wrinkles also grow at a faster rate. The wrinkle amplitude starts to grow faster around cycle 530 and, during the last 25 cycles, grows in a nearly exponential manner. The simulation was terminated after cycle 610 when the tube showed signs of eminent collapse. The average strain level at which similar tubes developed a limit load instability under monotonic loading ($\bar{\varepsilon}_{\mathrm{Lmon}}$) is seen once more to coincide with the strain level at which the rate of ratcheting experiences exponential growth. Figure 12(*b*) shows scaled renderings of the original tube geometry and of three deformed configurations corresponding to the cycle numbers indicated. $N=410$ corresponds to the end of the first phase of cycling. The wrinkles have formed, but they are barely discernible without amplification. By cycle 607, the wrinkles are fully formed and localization has started. The last configuration corresponds to $N=616$, which is past the termination of the experiment. Here, the localization is very clear, and to all intents and purposes the tube can be considered collapsed.

In summary then, the model with the set of parameters chosen is seen to reproduce with accuracy all aspects of this very nonlinear structural behavior, including the onset of buckling and localization instabilities. The other two cyclic experiments were also simulated using the same imperfection and constitutive model parameters (specimen geometric and loading cycle variables given in Table 2). The results are similar to those of experiment CWR19, and thus only the ratcheting predictions are shown in Fig. 13 along with the corresponding experimental results. The model is seen to replicate the ratcheting rate of δ_x^p in the first phase of these experiments very well. In the second phase the ratcheting rate is reproduced very well for CWR15 and somewhat less well for CWR18. In both cases, the final exponentially growing part of the record occurs at the same approximate level as in the experiments and the corresponding level at which the tube develops a limit load under uniaxial compression.

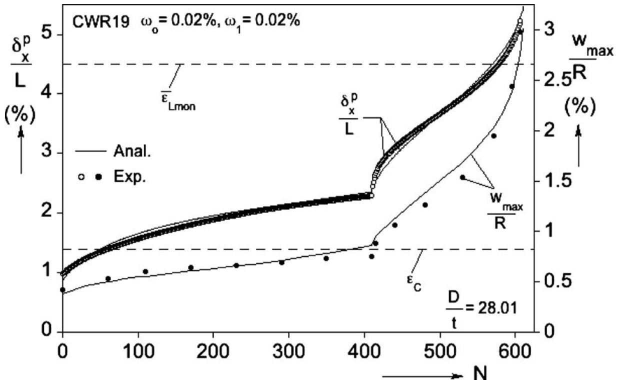

Fig. 11 Comparison of measured and calculated peak axial displacement and maximum radial displacement versus *N*

3.3 Sensitivity of Ratcheting to Key Model Parameters. The imperfection amplitudes and the constitutive model parameters adopted in the model for the conduct of the simulations above can influence the predictions. Jiao and Kyriakides [13] presented a detailed study of the effect of these parameters from which some general guidelines for the values that result in the optimal performance of the model in predicting the observed behavior were established. These guidelines formed also the basis for the present calculations, but some modifications had to be introduced to reflect the new cyclic loading conditions. Thus, for example, for the prewrinkled tubes cycled in Ref. [13] the imperfection amplitudes were $\{\omega_o, \omega_1\}=\{0.09, 0.09\}\%$. Here, the cycling was commenced well before any wrinkles developed. Consequently, the two amplitudes had to be reduced to $\{0.02, 0.02\}\%$ in order for the rate of ratcheting to be reproduced correctly. Figure 14 shows how these imperfection parameters affect the rate of growth of δ_x^p as a function of N for four values of imperfection amplitudes (0%, 0.02%, 0.05%, and 0.09%). In the absence of an imperfection ($\omega_o=\omega_1=0$), the tube does not wrinkle and the recorded shortening is strictly due to material strain ratcheting that is governed by constitutive model parameters. Despite this, during the first phase of the experiment ($N \leq 410$), the predictions remain very close to the measurements supporting the relatively slow growth of the wrinkle amplitude reported in the experiment. During the second phase of the test, wrinkle growth becomes more dominant, and the predictions are seen to underpredict the measurements. By contrast, when the imperfection amplitudes are assigned the value of 0.09%, the rate ratcheting in δ_x^p is overpredicted somewhat for $200 < N \leq 410$ and significantly subsequently. For imperfection amplitudes of 0.05%, the predictions are closer to the measurements but remain higher. The best predictions were yielded by $\omega_o=\omega_1=0.02\%$, which was adopted in the simulations presented in Sec. 3.2.

Figure 15 shows the effect of the *relaxation coefficient* C_r of the constitutive model (see Eq. (A7*b*)) on the predicted δ_x^p-N results for CWR19. Hassan et al. [12] pointed out that if the bound is kept fixed, the rate of ratcheting becomes progressively slower and can eventually lead to shakedown. This indeed is illustrated in Fig. 15 for $C_r=0$. The second term in Eq. (A7*b*) allows the bound

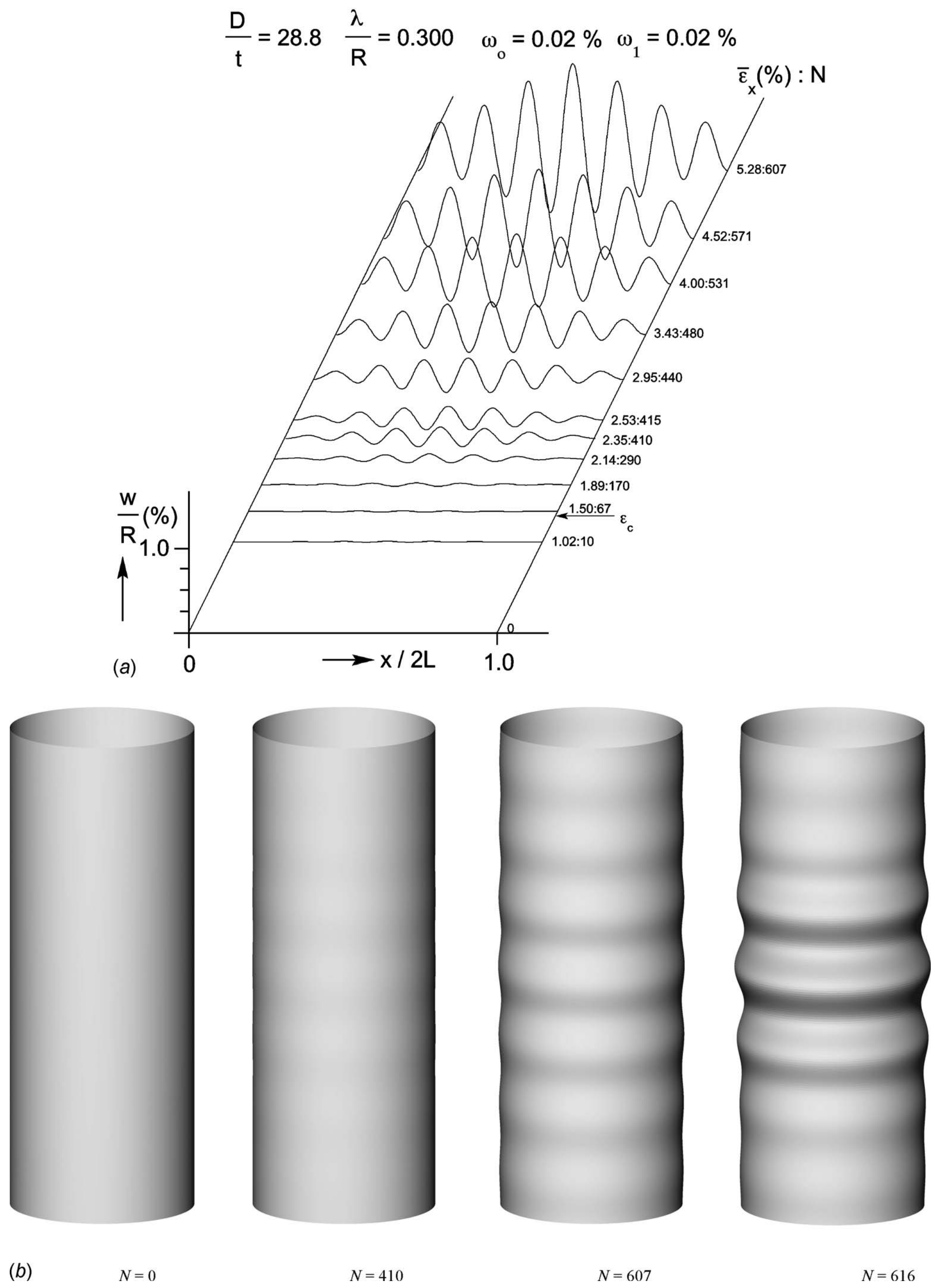

Fig. 12 (*a*) **Calculated radial displacement axial profiles after different numbers of cycles showing the growth and localization of wrinkles for CWR19.** (*b*) **The initial and three tube deformed configurations during the cyclic history.**

to shift downward or to relax (Hassan and Kyriakides [26,27]). The results in the figure demonstrate that as C_r increases, the rate of ratcheting increases. The value of 40 was found to best reproduce the rate of ratcheting in the tube geometry and material used in the present set of experiments. By contrast, $C_r = 60$ was adopted in Ref. [13] for the best simulation of the cyclic growth of wrinkles on prewrinkled tubes.

4 Conclusions

It is well known that axial stress-controlled cycling about a positive or negative mean stress can lead to the accumulation of deformation, also known as ratcheting. It is also well established that tubes thick enough to buckle in the plastic range under axial compression first develop axisymmetric wrinkles. With further compression, the wrinkle amplitude grows and gradually reduces the axial rigidity of the structure, eventually leading to a limit load instability that is followed by localization and collapse. This body of work aims to understand how wrinkling and ratcheting interact and the consequences of their interaction. In our preceding publication [13], we examined the response of tubes prewrinkled by compression to axial stress-controlled cycling about a compressive mean stress. We reported that this type of cycling causes simultaneous material ratcheting as well as growth of the amplitude of the wrinkles. As the average strain at which similar tubes

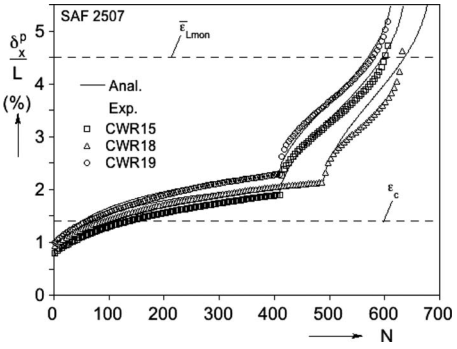

Fig. 13 Comparison of measured and calculated peak displacements per cycle versus *N* from three experiments with slightly different initial prestraining

start to collapse under monotonic loading is approached, the rate of growth of the wrinkles accelerates, and the tube experiences localized collapse. The rate of growth of the material ratcheting and of the wrinkles depends on the amplitude and mean stress of the applied cycles.

In the present study, tubes of the same geometry ($D/t \approx 28.7$) and material (SAF2507 super-duplex steel) were cycled in a similar manner, but the cycling was commenced at compressive strain levels that were much smaller than the value at which wrinkles first appear in the tubes. In other words, we started with an intact tube geometry. During the cycling, the surface of the tube was periodically scanned with a very sensitive laser displacement transducer for signs of nontrivial deformation. It was found that initially the tube shortened uniformly due to pure material ratcheting. At some stage, small amplitude nonuniformities started appearing on the surface of the tube, which gradually organized themselves into axisymmetric wrinkles. Interestingly, the wavelengths of such wrinkles were approximately the same as those of wrinkles formed under monotonic compression. Even more importantly, the strain levels at which they appeared coincided with the critical wrinkling strain levels measured under monotonic loading. This happened despite the fact that the maximum compressive stress of the cycles was smaller than the bifurcation stress under pure compression. In other words, the onset of wrinkling appears to be strain rather than stress driven, a result that is contrary to the hitherto general understanding that plastic bifurcation buckling is stress driven.

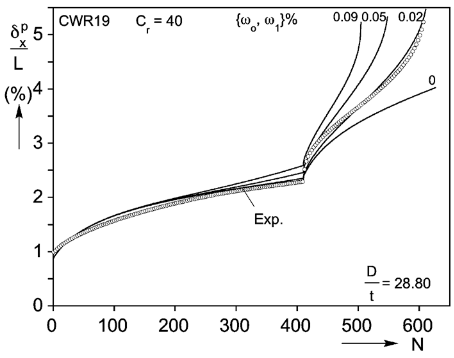

Fig. 14 Effect of imperfection parameters on calculated $\delta_x^p - N$ ratcheting response

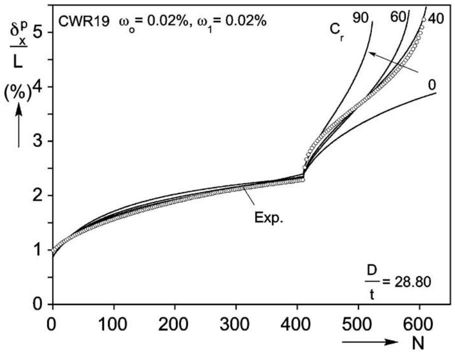

Fig. 15 Effect of relaxation coefficient C_r on calculated $\delta_x^p - N$ ratcheting response

Once the wrinkles are thus formed, further cycling causes growth of their amplitude. The wrinkle growth degrades the structure and eventually leads to localization and collapse. In concert with the results reported in Ref. [13], collapse under cyclic loading was found to occur when the average strain in the tube reached a level that corresponds to the average strain at the load maximum under monotonic loading. In other words, the localization and collapse are also strain rather than stress driven. The number of cycles required for both the wrinkling and collapse instabilities to develop is governed first by the level of the initial prestrain and second by the mean stress and amplitude of the load cycles.

The experiments were simulated numerically using nonlinear axisymmetric shell kinematics and the two-surface plasticity model of Dafalias and Popov [24,25] together with the modifications required for ratcheting applications of Hassan et al. [12] and Hassan and Kyriakides [11,26,27]. The shell domain analyzed was assigned very small initial axisymmetric imperfections with a small axial bias in order to facilitate localization. The amplitudes of these imperfections were chosen for optimal performance of the model in predicting the rate of ratcheting and the onset of localization. The plasticity model was calibrated to measured stress-strain data of the stainless steel used in the experiments. The numerical model reproduced with accuracy the initial pure material ratcheting. The imperfection amplitude initially grew insignificantly but much faster when the induced strain reached the level at which the tube bifurcates into the wrinkling mode under pure compression, confirming the experimental observations. Once formed, the wrinkle amplitude grew with cycling and eventually led to localization and collapse. It was again confirmed that collapse under cyclic loadings materializes when the wrinkles reach a critical level and that the average strain at collapse corresponds to that at the onset of collapse under monotonic loading.

Acknowledgment

The authors acknowledge with thanks the financial support of the work received from a consortium of industrial sponsors under the project Structural Integrity of Offshore Pipelines. Preliminary experiments initiated by Ralf Peek aimed to investigate the potential of buckling under cyclic loadings experienced by hot buried pipelines were conducted in 2002–2004 by E. Corona and S. Kyriakides.

Appendix: Outline of Two-Surface Model of Dafalias and Popov [24,25]

The material is cyclically stable so the yield surface (YS) retains its size (σ_o) and shape and, in terms of the stress $\boldsymbol{\sigma}$ and back stress $\boldsymbol{\alpha}$, is given by

$$f(\boldsymbol{\sigma}-\boldsymbol{\alpha})=\left[\tfrac{3}{2}(\boldsymbol{s}-\boldsymbol{a})\cdot(\boldsymbol{s}-\boldsymbol{a})\right]^{1/2}=\sigma_o \tag{A1}$$

where $\boldsymbol{s}$ and $\boldsymbol{a}$ are, respectively, the deviators of $\boldsymbol{\sigma}$ and $\boldsymbol{\alpha}$. The yield surface is surrounded by a geometrically similar bounding surface (BS) of size σ_b (see Fig. 16) defined by

$$F(\overline{\boldsymbol{\sigma}}-\boldsymbol{\beta})=\left[\tfrac{3}{2}(\overline{\boldsymbol{s}}-\boldsymbol{b})\cdot(\overline{\boldsymbol{s}}-\boldsymbol{b})\right]^{1/2}=\sigma_b \tag{A2}$$

Here, $\overline{\boldsymbol{\sigma}}$ is the congruent point on the BS to $\boldsymbol{\sigma}$ on the YS, $\boldsymbol{\beta}$ is the center of the BS, and $\overline{\boldsymbol{s}}$ and $\boldsymbol{b}$ are, respectively, their deviators. An

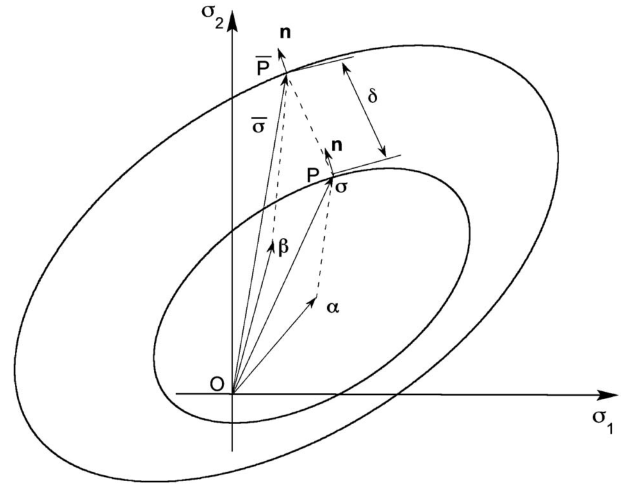

Fig. 16 Yield and bounding surfaces and associated variables of the Dafalias–Popov model

associative flow rule is assumed so plastic strain increments are given by

$$d\boldsymbol{\varepsilon}^p = \frac{1}{H}\left(\frac{\partial f}{\partial \boldsymbol{\sigma}} \cdot d\boldsymbol{\sigma}\right)\frac{\partial f}{\partial \boldsymbol{\sigma}} \tag{A3}$$

The plastic modulus H is related to the distance δ of the current stress on the YS (**P**) from its congruent point on the BS ($\overline{\mathbf{P}}$, Fig. 16) through

$$H(\delta, \delta_{in}) = E_o^p + h\left(\frac{\delta}{\delta_{in} - \delta}\right) \tag{A4a}$$

where E_o^p is the modulus of the bound, δ_{in} is the value of δ at the last elastic state, and h will be taken as

$$h = \frac{a}{1 + b(\delta_{in}/2\sigma_b)^\gamma} \tag{A4b}$$

(a, b, and γ are material constants). Furthermore the scalar δ is given by (see Fig. 16)

$$\delta = [(\overline{\boldsymbol{\sigma}} - \boldsymbol{\sigma}) \cdot (\overline{\boldsymbol{\sigma}} - \boldsymbol{\sigma})]^{1/2} \tag{A5}$$

The YS translates in stress space according to the following hardening rule (Armstrong–Frederick [28], Hassan et al. [12], and Hassan and Kyriakides [27]):

$$d\boldsymbol{\alpha} = d\mu \frac{[(1-k)(\boldsymbol{\sigma} - \boldsymbol{\alpha}) - k\boldsymbol{\alpha}]}{|(1-k)(\boldsymbol{\sigma} - \boldsymbol{\alpha}) - k\boldsymbol{\alpha}|} \tag{A6}$$

The translation of the BS is coupled to that of the YS as follows:

$$d\boldsymbol{\beta} = d\boldsymbol{\alpha} - dM\frac{(\overline{\boldsymbol{\sigma}} - \boldsymbol{\sigma})}{|\overline{\boldsymbol{\sigma}} - \boldsymbol{\sigma}|}, \quad dM = \left(1 - \frac{E_b^p}{H}\right)\left(\frac{d\boldsymbol{\sigma} \cdot \boldsymbol{n}}{\boldsymbol{m} \cdot \boldsymbol{n}}\right) \tag{A7a}$$

and

$$E_b^p = E_o^p + C_r[(\boldsymbol{b} \cdot \boldsymbol{b})^{1/2} - \boldsymbol{b} \cdot \boldsymbol{n}] \tag{A7b}$$

(for more details on Eqs. (A6) and (A7*b*), see Hassan and Kyriakides [26,27]). Finally, the tubes tested exhibit some plastic anisotropy that is introduced, as described in Ref. [13]. The numerical implementation of the model follows along the lines of the subroutine of Kyriakides and Corona [29].

References

[1] Lee, L. H. N., 1962, "Inelastic Buckling of Initially Imperfect Cylindrical Shells Subject to Axial Compression," J. Aerosp. Sci., **29**, pp. 87–95.
[2] Batterman, S. C., 1965, "Plastic Buckling of Axially Compressed Cylindrical Shells," AIAA J., **3**(2), pp. 316–325.
[3] Gellin, S., 1979, "Effect of an Axisymmetric Imperfection on the Plastic Buckling of an Axially Compressed Cylindrical Shell," ASME J. Appl. Mech., **46**, pp. 125–131.
[4] Bushnell, D., 1982, "Plastic Buckling of Various Shells," ASME J. Pressure Vessel Technol., **104**, pp. 51–72.
[5] Tvergaard, V., 1983, "Plastic Buckling of Axially Compressed Circular Cylindrical Shells," Thin-Walled Struct., **1**, pp. 139–163.
[6] Tvergaard, V., 1983, "On the Transition From a Diamond Mode to an Axisymmetric Mode of Collapse in Cylindrical Shells," Int. J. Solids Struct., **19**, pp. 845–856.
[7] Yun, H. D., and Kyriakides, S., 1990, "On the Beam and Shell Modes of Buckling of Buried Pipelines," Soil. Dyn. Earthquake Eng., **9**, pp. 179–193.
[8] Bardi, F. C., and Kyriakides, S., 2006, "Plastic Buckling of Circular Tubes Under Axial Compression—Part I: Experiments," Int. J. Mech. Sci., **48**, pp. 830–841.
[9] Bardi, F. C., Kyriakides, S., and Yun, H. D., 2006, "Plastic Buckling of Circular Tubes Under Axial Compression—Part II: Analysis," Int. J. Mech. Sci., **48**, pp. 842–854.
[10] Kyriakides, S., and Corona, E., 2007, *Mechanics of Offshore Pipelines, Volume 1: Buckling and Collapse*, Elsevier, Oxford, UK.
[11] Hassan, T., and Kyriakides, S., 1992, "Ratcheting in Cyclic Plasticity—Part I: Uniaxial Behavior," Int. J. Plast., **8**, pp. 91–116.
[12] Hassan, T., Corona, E., and Kyriakides, S., 1992, "Ratcheting in Cyclic Plasticity—Part II: Multiaxial Behavior," Int. J. Plast., **8**, pp. 117–146.
[13] Jiao, R., and Kyriakides, S., 2009, "Ratcheting, Wrinkling and Collapse of Tubes Under Axial Cycling," Int. J. Solids Struct., **46**, pp. 2856–2870.
[14] Klever, F. J., Palmer, A. C., and Kyriakides, S., 1994, "Limit-State Design of High-Temperature Pipelines," *Proceedings of the 13th International Conference on Offshore Mechanics and Arctic Engineering*, Houston, TX, Feb. Vol. V, pp. 77–92.
[15] Kyriakides, S., and Shaw, P. K., 1987, "Inelastic Buckling of Tubes Under Cyclic Bending," ASME J. Pressure Vessel Technol., **109**, pp. 169–178.
[16] Corona, E., and Kyriakides, S., 1991, "Experimental Investigation of the Degradation and Buckling of Circular Tubes Under Cyclic Bending and External Pressure," Thin-Walled Struct., **12**, pp. 229–263.
[17] Chang, K.-H., and Pan, W.-F., 2009, "Buckling Life Estimation of Circular Tubes Under Cyclic Bending," Int. J. Solids Struct., **46**, pp. 254–270.
[18] Ellison, M. S., and Corona, E., 1998, "Buckling of T-Beams Under Cyclic Bending," Int. J. Mech. Sci., **40**, pp. 835–855.
[19] Vaze, S., and Corona, E., 1998, "Degradation and Collapse of Square Tubes Under Cyclic Bending," Thin-Walled Struct., **31**, pp. 325–341.
[20] Yin, S., Corona, E., and Ellison, M., 2004, "Degradation and Buckling of I-Beams Under Cyclic Pure Bending," J. Eng. Mech., **130**, pp. 809–817.
[21] Goto, Y., Toba, Y., and Matsuoka, H., 1995, "Localization of Plastic Buckling Patterns Under Cyclic Loading," J. Eng. Mech., **121**(4), pp. 493–501.
[22] Corona, E., 2005, "Buckling Mode Localization in Restrained Columns Under Cyclic Loading," ASME J. Appl. Mech., **72**, pp. 620–622.
[23] Kyriakides, S., Bardi, F. C., and Paquette, J. A., 2005, "Wrinkling of Circular Tubes Under Axial Compression: Effect of Anisotropy," ASME J. Appl. Mech., **72**, pp. 301–305.
[24] Dafalias, Y. F., and Popov, E. P., 1975, "A Model of Nonlinearly Hardening Materials for Complex Loading," Acta Mech., **21**, pp. 173–192.
[25] Dafalias, Y. F., and Popov, E. P., 1976, "Plastic Internal Variables Formalism of Cyclic Plasticity," ASME J. Appl. Mech., **43**, pp. 645–651.
[26] Hassan, T., and Kyriakides, S., 1994, "Ratcheting of Cyclically Hardening and Softening Materials: I. Uniaxial Behavior," Int. J. Plast., **10**, pp. 149–184.
[27] Hassan, T., and Kyriakides, S., 1994, "Ratcheting of Cyclically Hardening and Softening Materials: II. Multiaxial Behavior," Int. J. Plast., **10**, pp. 185–212.
[28] Armstrong, P. J., and Frederick, C. O., 1966, "A Mathematical Representation of the Multiaxial Bauschinger Effect," Berkeley Nuclear Laboratories, R&D Department, Report No. RD/B/N/731.
[29] Kyriakides, S., and Corona, E., 1995, "Cyclic Plasticity Routines (CYPROUS)," Proprietary software, Mechanica Report No. 95/1.